

# On the feasibility of monitoring Carbon Monoxide in the lower troposphere from a constellation of Northern Hemisphere geostationary satellites. (PART 1)

Jérôme Barré<sup>1</sup>, David Edwards<sup>1</sup>, Helen Worden<sup>1</sup>, Arlindo Da Silva<sup>2</sup>, William Lahoz<sup>3</sup>

<sup>1</sup> National Center for Atmospheric Research (NCAR), Boulder, CO, USA

<sup>2</sup> NASA Goddard Space Flight Center, Greenbelt, MD, USA

<sup>3</sup> NILU, Kjeller, Norway

Corresponding Author:

Jérôme Barré, Phone: 303-497-1866, Fax: 303-497-1400

*barre@ucar.edu*

## Abstract

By the end of the current decade, there are plans to deploy several geostationary Earth orbit (GEO) satellite missions for atmospheric composition over North America, East Asia and Europe with additional missions proposed. Together, these present the possibility of a constellation of geostationary platforms to achieve continuous time-resolved high-density observations over continental domains for mapping pollutant sources and variability at diurnal and local scales. In this paper, we use a novel approach to sample a very high global resolution model (GEOS-5 at 7 km horizontal resolution) to produce a dataset of synthetic carbon monoxide pollution observations representative of those potentially obtainable from a GEO satellite constellation with predicted measurement sensitivities based on current remote sensing capabilities. Part 1 of this study focuses on the production of simulated synthetic measurements for air quality OSSEs (Observing System Simulation Experiments). We simulate carbon monoxide nadir retrievals using a technique that provides realistic measurements with very low computational cost. We discuss the sampling methodology: the projection of footprints and areas of regard for geostationary geometries over each of the North America, East Asia and Europe regions; the regression method to simulate measurement sensitivity; and the measurement error simulation. A detailed analysis of the simulated observation sensitivity is performed, and limitations of the method are discussed. We also describe impacts from clouds, showing that the efficiency of an instrument making atmospheric composition measurements on a geostationary platform is dependent on the dominant weather regime over a given region and the pixel size resolution. These results demonstrate the viability of the “instrument simulator” step for an OSSE to assess the performance of a constellation of geostationary satellites for air quality measurements. We describe the OSSE results in a follow up paper (Part 2 of this study).

43

## 44 1. Introduction

45

46 Current satellite observations of tropospheric composition made from low  
47 Earth orbit (LEO) satellites provide at best one or two measurements each day at  
48 any given location. Coverage is quasi-global but sparse, often with large  
49 uncertainties in individual measurements that limit examination of local and  
50 regional atmospheric composition over short time periods. This has hindered the  
51 operational uptake of these data for monitoring air quality and population exposure,  
52 and for initializing and evaluating chemical weather forecasts.

53

54 By the end of the current decade, there are planned geostationary Earth orbit  
55 (GEO) satellite missions for atmospheric composition over North America, East Asia  
56 and Europe, with additional missions proposed (CEOS, 2011). Together, these  
57 present the possibility of a constellation of GEO platforms to achieve continuous  
58 time-resolved high-density observations over continental domains for mapping  
59 pollutant sources and variability. The GEO geometry provides a continuous view of  
60 the part of the Earth that is below the satellite, enabling measurements many times  
61 per day that help capture the diurnal evolution of emission sources, tropospheric  
62 chemistry and pollution transport.

62

63 The planned GEO missions include the EVI-1/TEMPO (Tropospheric  
64 Emission: Monitoring of Pollution, Zoogman et al., 2014b) over USA, Sentinel 4/IRS  
65 over Europe and GEMS over Asia. Each mission has a different primary objective,  
66 but they share the common goal of monitoring pollutants for atmospheric  
67 composition and air quality and will have a common measurement capability for  
68 ozone ( $O_3$ ), nitrogen dioxide ( $NO_2$ ), sulfur dioxide ( $SO_2$ ), formaldehyde (HCHO) and  
69 aerosols, utilizing radiances in the ultraviolet-visible (UV-Vis) spectrum. Planned  
70 GEO observations of infrared active trace gases of relevance to air quality are  
71 currently limited to total column carbon monoxide (CO) observations from the  
72 European IRS instrument, which is originally not driven by atmospheric  
73 composition applications. However, other IR measurements that could play a part in  
74 the GEO constellation are being proposed as part of the NASA Decadal Survey GEO-  
75 CAPE (GEOstationary Coastal and Air Pollution Events) mission, such as the EVI-3  
76 CHRONOS mission (<https://www2.acd.ucar.edu/chronos>) that would measure CO  
77 and methane ( $CH_4$ ) using heritage from the Terra/MOPITT (Measurement of  
78 Pollution in The Troposphere) instrument. Given the effect of nearby emissions and  
79 transported pollution on local air quality, MOPITT-like CO observations are a good  
80 candidate for air quality measurements on a GEO platform because the unique  
81 sensitivity of this platform to pollution in the boundary layer, as well as in the free  
82 troposphere, allows both vertical and horizontal tracking of pollution transport.

82

83 Carbon monoxide is a primary pollutant and plays an important role in  
84 tropospheric chemistry and its sources are both natural and anthropogenic. There  
85 are two main processes of CO production: incomplete combustion (e.g., industrial  
86 and urban fossil/bio fuel burning, wildfires and biomass burning); and natural  
87 chemical production from hydrocarbon oxidation. As an  $O_3$  precursor, CO is also  
88 important in determining the tropospheric  $O_3$  budget. The principal CO sink is the  
89 oxidation by hydroxyl (OH) radicals, giving an average CO lifetime of about two  
90 months dependent on season. With these characteristics, CO serves as a tracer of

90 pollution emissions and transport, and as a proxy for emissions and distributions of  
91 other species co-emitted with CO but not easily measured. Taken together,  
92 observations of the full suite of UV-Vis and IR trace gases and aerosols could provide  
93 the high spatio-temporal resolution continental-scale observations of lower-  
94 tropospheric pollution needed to monitor, forecast, and manage air quality on a  
95 daily basis (Edwards et al., 2009; Lahoz et al., 2012; Bowman et al. 2013).

96 Previous GEO observation simulation studies for air quality have assessed  
97 the potential capabilities of instruments covering the above three continental  
98 regions separately. Edwards et al. (2009) and Zoogman et al. (2011, 2014ab)  
99 consider the CONUS (continental US) region and demonstrate the feasibility of using  
100 observing system simulation experiment (OSSE) studies to help define quantitative  
101 trace gas measurement requirements in different spectral regions for satellite  
102 missions and to evaluate the expected performance of proposed observing  
103 strategies to test the ability of GEO satellite measurements of ozone (O<sub>3</sub>) and CO.  
104 Claeys et al. (2011) and Sellitto et al. (2013b) cover the European region and  
105 describe the capabilities of a concept nadir thermal infrared sensor proposed for  
106 deployment onboard a GEO platform to monitor O<sub>3</sub> and CO for air quality purposes  
107 (MAGEAQ: Monitoring the Atmosphere from Geostationary orbit for European Air  
108 Quality). Lastly, Zoogman et al. (2014a) assimilate concurrent ozone and CO  
109 observations and show that geostationary measurement of CO provides significant  
110 benefit for monitoring ozone.

111 The goal of this study is to evaluate the impact of a future GEO constellation  
112 on global chemical weather by using the observing system simulation experiment  
113 (OSSE) technique. Here we primarily consider CO as a good chemical tracer for  
114 evaluating the impact of a GEO constellation of observations. As described by  
115 Edwards et al. (2009), chemical OSSEs provide a way of expanding case-specific  
116 sensitivity studies to assess the impact of future measurements systems. A chemical  
117 OSSE is composed of several elements (fig. 1 – see also, Timmermans et al., 2014). A  
118 nature run (NR) (1) represents the atmospheric true state. A complete OSSE needs  
119 an observation simulator (2) to sample the nature run to produce synthetic  
120 observations (3). The synthetic observations are then assimilated using a data  
121 assimilation system (4) into a second atmospheric model, the control run (CR) (5).  
122 This produces the assimilation run (AR) (6). The impact of concept instrument  
123 measurements on constraining the modeled state of the atmosphere can then be  
124 evaluated and assessed (7) by comparing the NR, CR and AR (1, 5 and 6). We  
125 describe this study in two parts. In the present paper (Part 1) we focus on the NR  
126 (1), observation simulator (2) and synthetic observations (3). A follow-up article  
127 (Part 2) will focus on assimilating the simulated measurements and assessing the  
128 synergies between the different instruments of the constellation by simulating data-  
129 denial case studies (elements 4 to 7 in fig. 1). This study presents for the first time a  
130 global GEO constellation OSSE for CO.

131 According to Rodgers (2000), within the remote sensing optimal estimation  
132 framework one can represent the sensitivity of the retrieved trace gas profile from a  
133 satellite measurement to the true state of the atmosphere by the averaging kernel  
134 (AK) function. For accurate observation simulations in an OSSE, we need a full  
135 radiative transfer model for radiances and their Jacobians (which represent the  
136 sensitivity of the radiance to the true atmospheric state) to compute the AKs for

137 each atmospheric and surface scene. Since this presents a significant computational  
138 burden, practical implementations of OSSEs for air quality to date have used  
139 approximated observation simulators. Some have used specified constant AKs  
140 (Edwards et al., 2009; Zoogman et al., 2011), or have simplified the AK variability by  
141 considering only a few scene types (Claeyman et al., 2011). Sellitto et al. (2013a)  
142 showed that the use of no, or limited scene dependent AK, parameterizations could  
143 significantly misrepresent the sensitivity of an observing system. Sellitto et al.  
144 (2013a) also recommend using comprehensive scene-dependent approximations of  
145 the AKs in cases where the computational cost of a full radiative transfer model is  
146 too expensive to perform an OSSE study (for example, for a GEO constellation).  
147 Worden et al. (2013) address this issue by using a multiple regression analysis of  
148 real satellite observations to estimate scene-dependent averaging kernels, thus  
149 avoiding the use of a full radiative transfer model. This method allows the fast  
150 computation of scene-dependent AKs, and the processing of a very large dataset of  
151 synthetic observations in a short amount of time.

152 Due to the constraint from the NR space and time resolution, approximations  
153 made to the instrument sampling and horizontal resolution cannot provide  
154 information at a higher resolution than the nature run (Edwards et al., 2009). One  
155 should use high space and time resolution NRs to simulate high instrument space  
156 and time sampling. The planned missions mentioned above would provide less than  
157 10 km spatial resolution at about every 1 hour. Sellitto et al. (2013b) also  
158 approximated the observation simulation by not discarding the cloud-contaminated  
159 measurements, thus leading to a possible overestimation of the GEO instrument  
160 potential to monitor tropospheric O<sub>3</sub> and pollution features in general. One should  
161 account for cloud contamination by testing scenarios with variable instrument  
162 sampling and resolution.

163 In this paper we use the multiple regression analysis of Worden et al. (2013)  
164 to produce a very large data set representing a GEO constellation of synthetic  
165 observations for air quality. In section 2, we describe the very high resolution NR  
166 from the Goddard Earth Observing System Model version 5 (GEOS-5) at 7 km  
167 horizontal resolution. Section 3 describes the sampling methodology with details on  
168 the geostationary projection to the surface of the earth, and the multi linear  
169 regression method with its limitations for predicting averaging kernels and  
170 estimated observation errors. Section 4 investigates the impacts of clouds on the  
171 GEO constellation. The effect of horizontal resolution and sampling is discussed.  
172 Section 5 presents the measurements and a detailed analysis of the simulated  
173 observation sensitivity (e.g., averaging kernel variability). Section 6 gives a  
174 summary, conclusions and perspectives.

175

## 176 2. The nature run

177

178 The Goddard Earth Observing System Model, Version 5 (GEOS-5, Rienecker et  
179 al., 2008) is used to provide the NR. The GEOS-5 atmospheric model is a weather-  
180 and-climate model used for atmospheric analyses, weather forecasts, uncoupled and  
181 coupled climate simulations and predictions, and for coupled chemistry-climate  
182 simulations. The NR used for this study covers a 2-year global, non-hydrostatic  
183 mesoscale simulation for the period 2005-2006. In addition to standard

184 meteorological parameters (wind, temperature, moisture, surface pressure), this  
185 simulation includes 15 aerosols tracers (dust, sea salt, sulfate, black and organic  
186 carbon), and O<sub>3</sub>, CO and carbon dioxide (CO<sub>2</sub>) trace gases.

187 The model simulation is driven by prescribed sea-surface temperature and  
188 sea-ice derived at a horizontal resolution of 0.25 degrees. Biomass burning  
189 emissions of organic carbon, sulfate, CO and CO<sub>2</sub> are obtained from the Quick Fire  
190 Emissions Dataset (QFED) version 2.4-r6. The basis of the QFED is the fire radiative  
191 power (top-down) approach, and it draws on the cloud correction method used in  
192 the Global Fire Assimilation System (GFAS; Kaiser et al. 2012). Anthropogenic  
193 emissions of carbon species and aerosols are largely taken from the Emissions  
194 Database for Global Atmospheric Research (EDGAR; Olivier et al., 1994), which are  
195 provided annually at a resolution of 0.1 degrees. For CO and CO<sub>2</sub>, EDGAR v4.2  
196 emissions from 2005 through 2007 were used. For organic and black carbon  
197 aerosols species, Hemispheric Transport of Air Pollution (HTAP) emissions were  
198 used.

199 Outputs at 30-minute intervals have been produced at a resolution of 0.0625  
200 degrees (~7 km) using a cubed-sphere horizontal grid with 72 vertical levels,  
201 extending from the surface up to 0.01 hPa (~85 km). All details and references  
202 concerning nature run file specifications, meteorology, chemistry and emissions can  
203 be found in the NR description documents at:  
204 <http://gmao.gsfc.nasa.gov/projects/G5NR/>

205 In this study we focus on July 2006. Figure 2 shows the CO total column  
206 provided by the NR for 15 July 2006 at 15:00 UT. This map shows the ability of the  
207 NR to represent the high variability of CO fields at a global scale. We display typical  
208 and expected CO values: very high values (above  $4.10^{18}$  molecules/cm<sup>2</sup>) over central  
209 Africa due to biomass burning; high values (around  $3.10^{18}$  molecules/cm<sup>2</sup>) over  
210 dense populated areas due to anthropogenic emissions. The NR total columns of CO  
211 also clearly show long-range transport patterns of CO from anthropogenic and  
212 biomass-burning sources across the oceans of the Northern Hemisphere (NH) and  
213 Southern Hemisphere (SH), respectively.

214 Figure 3 shows the July 2006 average of surface CO values over the three  
215 regions of interest (North America - CONUS, Europe and Eastern Asia). The NR  
216 shows realistic horizontal CO variability due to the very high space and time  
217 resolutions of the simulations. Emissions from cities from small to large size are  
218 clearly identifiable. Transport infrastructure such as roads (eastern US in figure 3.a)  
219 and ship routes (China sea in figure 3.c) are also visible. In this study we use the NR  
220 model output variables, both the chemical parameters (CO quantities) and the  
221 meteorological parameters (not shown), to predict averaging kernels for simulated  
222 observations in the GEO constellation. This is done for each of the CONUS, Europe  
223 and Eastern Asia regions of interest.

## 224 3. Sampling methodology

### 226 3.1. Geometry of measurements

228 We constructed three GEO instrument simulators over the three regions of  
229 interest defined immediately above using the methodology described in Worden et  
230

231 al. (2013). Footprints of the instruments are defined as a GEO projection on the  
 232 globe. We defined  $x$  (along the parallel from the sub-satellite point) and  $y$  (along the  
 233 meridian from the sub-satellite point) at regularly spaced scanning angles (in  
 234 degrees). The GEO projection consists of projecting these angles from the GEO  
 235 platform to the surface of the earth to obtain the corresponding longitudes and  
 236 latitudes of the footprints. We have the following relationship between viewing  
 237 angles at the satellite location and latitude, longitude position on the earth surface:

238

$$239 \quad lon = \tan^{-1}(s_1/s_2) + sub\_lon \quad (1)$$

240

$$241 \quad lat = \tan^{-1}(p_2(s_3/s_{xy})) \quad (2)$$

242

243 where  $sub\_lon$  is the sub-satellite point longitude and:

244

$$245 \quad s_1 = p_1 - s_n \cos x \cos y$$

246

$$247 \quad s_2 = s_n \sin x \cos y$$

248

$$249 \quad s_3 = -s_n \sin y$$

250

$$251 \quad s_{xy} = \sqrt{s_1^2 + s_2^2}$$

252

$$253 \quad s_d = \sqrt{(p_1 \cos x \cos y)^2 - ((\cos y)^2 + p_2(\sin y)^2)p_3}$$

254

$$255 \quad s_n = \frac{p_1 \cos x \cos y - s_d}{(\cos y)^2 + p_2(\sin y)^2}$$

256

257  $p_1 = 42164$  km, the altitude of a GEO platform from the center of the earth

258  $p_2 = 1.006803$  is the ratio of the earth radius at the equator and at the pole ( $p_2 =$   
 259  $r_{eq}/r_{po}$ ).

260  $p_3 = p_1^2 - r_{eq}^2$

261

262 These equations follow from the methods provided in the technical  
 263 document EUMETSAT (2011) and sketch of figure 4.d should be consulted to  
 264 understand the above formulas. Projecting the regularly spaced instrument viewing  
 265 angles onto the surface of the earth (figure 4.b) results in GEO instrument footprints  
 266 with non-regular latitude and longitude spacing. GEO instruments then have a non-  
 267 uniform horizontal resolution: the footprint density per surface area decreases as  
 268 the measurements go outward from the sub-satellite point (figure 4.c). The GEO-  
 CAPE concept mission (Fishman et al., 2012) requires hourly measurements with a  
 spatial resolution in the order of 5 to 10 km and a measurement domain of at least  
 5000 km. Table 1 gives an overview of the characteristics of the three instruments  
 that we call hereafter GEO-US (over CONUS), GEO-EU (over Europe) and GEO-AS  
 (over Eastern Asia). We set the scanning angles of the three instruments to have a  
 horizontal resolution under 10 km ( $0.1^\circ$ ) in the approximate middle of the

269 measurement domain (i.e., sub-longitude and the mean of latitudes at the sub-  
 270 longitude). Figure 4.a. shows the measurement domains of the GEO constellation.  
 271 Areas of coverage have different shapes due to the latitudinal extent of continents;  
 272 GEO-EU has more of a latitudinal extent compared to GEO-US, which has to cover a  
 273 wider longitude range. GEO-AS has been designed as a compromise solution  
 274 between measurements over Chinese mega-cities and measurements over Korea  
 275 and Japan.

276

277 3.2 Carbon monoxide instrument simulator

278

279 In this study, we assume characteristics of the CO measurements of the  
 280 troposphere similar to those of the Terra/MOPITT (Measurement of Pollution in the  
 281 Troposphere) instrument (Drummond, 1992). The last version of the retrieved CO  
 282 product version 5 (Deeter et al., 2013) uses a multispectral approach utilizing near-  
 283 visible infrared (NIR) solar backscatter signals at 2.3 microns and thermal infrared  
 284 (TIR) emission signals from the Earth surface and atmosphere at 4.6 microns. This  
 285 approach provides enhanced measurement sensitivity to near-surface CO  
 286 concentrations and allows the possibility of retrieving CO profile information to  
 287 separate CO in the planetary boundary layer and free troposphere (Worden et al.,  
 288 2010). This is a requirement for the GEO-CAPE concept mission (Fishman et al.,  
 289 2012) and it is generally desirable for air quality space remote observations to  
 290 distinguish between local emissions and transported pollution at a given location  
 291 (Lahoz et al., 2012). In the case of MOPITT, the combination of the TIR and NIR  
 292 radiances significantly improves the sensitivity to the lower tropospheric CO for  
 293 daytime land observations. For nighttime land and day/night ocean observations,  
 294 only the TIR radiances contribute to the retrieval.

295 The MOPITT-retrieved CO volume mixing ratios (VMRs) are on 10 pressure  
 296 levels (surface, 900, 800, 700, 600, 500, 400, 300, 200, 100 hPa). Each retrieved  
 297 level is representative of the layer content defined by the level value itself and the  
 298 level above. The top most level extends from 100 hPa to 50 hPa. The retrieved CO  
 299 profile  $y_r$  can be related to the true atmospheric state  $y_t$  with the following linear  
 300 relationship:

301

302

303

$$y_r = y_a + A(y_t - y_a) + \epsilon \quad (3)$$

304 In Eq. (3)  $y_t$  is the true atmospheric CO profile state (in  $\log_{10}(\text{VMR})$ ) and  $y_a$  is the a-  
 305 priori state vector (in  $\log_{10}(\text{VMR})$ ) derived from a monthly mean climatological  
 306 profile from the MOZART-4 (Model for Ozone and Related chemical Tracers, version  
 307 4) chemical transport model (Emmons et al., 2010). The random error  $\epsilon$  (in  
 308  $\log_{10}(\text{VMR})$ ) is simulated using the retrieval noise, and  $A$  is the retrieval AK matrix  
 309 (see section 3.3). (The  $y_r$  retrieved profile obtained is then converted from  
 310  $\log_{10}(\text{VMR})$  to VMR for the final data product).

311 Figure 5 shows two representative MOPITT AKs. The sensitivity of the  
 312 MOPITT instrument to near-surface CO varies according to different surface types  
 313 and atmospheric conditions. The left panel of Fig. 5 shows a typical AK for a daytime  
 314 measurement over land with enhanced sensitivity toward the surface. The right  
 315 panel of Fig. 5 shows a typical AK for a TIR-only ocean or nighttime measurement

316 over land with low sensitivity in the lowermost troposphere. A useful quantity  
 317 indicating the information content of a measurement is the degrees of freedom for  
 318 signal (DFS), given by  $tr(\mathbf{A})$  (Rodgers, 2000). Higher DFS values indicate more  
 319 sensitivity of the retrieval to the true profile.

320 To diagnose the sensitivity of the measurement to the lowest layers, DFS can  
 321 be calculated over the three lowest levels (Surface to 700 hPa) as  $DFS_{0,3} = \sum_{i=1}^3 A_{ii}$ .  
 322 In Figure 5 the DFS ( $DFS_{0,3}$ ) is 1.9 (0.7) and 1.5 (0.2) for land-day and ocean-night  
 323 measurements, respectively. We can see that MOPITT sensitivity toward the surface  
 324 ( $DFS_{0,3}$ ) is scene dependent. That is, it depends on various land and atmospheric  
 325 parameters (i.e., nature of the surface and current state of the atmosphere at a given  
 326 time) that control, among other things, the surface-atmospheric thermal contrast,  
 327 i.e., the difference between the surface temperature and the atmospheric  
 328 temperature profile.

329

330 3.3 Simulated retrieval method.

331

332 Worden et al. (2013) investigated the CO retrieval error resulting from the  
 333 use of a single average AK in an observation simulator compared using the true  
 334 retrieval AKs. They further developed a scene-dependent AK prediction tool capable  
 335 of approximating the true AK with a significant reduction in retrieved CO error  
 336 compared to using a single average AK. This AK prediction tool allows us to produce  
 337 a large amount of simulated data over months in an efficient manner. One month of  
 338 data for a GEO constellation (i.e., around 200 million profiles) can be produced in  
 339 less than 12 hours.

340 The method of Worden et al. employs a multiple regression approach for  
 341 deriving scene dependent AKs using predictors based on state parameters from the  
 342 NR. The main parameters used are: CO concentration, temperature, specific  
 343 humidity and pressure (see table 2). The method is based on the computation of the  
 344 singular value decomposition (SVD) of the AK matrix. Given an AK matrix  $\mathbf{A}$ , we  
 345 compute the SVD by means of:

346

$$347 \quad \mathbf{A} = \mathbf{U}\mathbf{\Lambda}\mathbf{V}^T \quad (4)$$

348

349 where the columns of  $\mathbf{U}$  and  $\mathbf{V}$  are the left and right singular vectors respectively,  
 350 and the elements of  $\mathbf{\Lambda}$  (a diagonal matrix) are the singular values. Since the first two  
 351 singular vectors account for 95% of the variability of MOPITT CO AKs on average  
 352 and the first three singular vectors account for 99.995 %, the method retains the  
 353 first three ranked singular vectors. For a complete description of the SVD technique,  
 354 numerical examples and software used please refer to Worden et al., 2013. We then  
 355 calculate the three first singular vectors and values using multiple regression. For  
 356 example,

357

$$358 \quad U_{ij} = c_{ij} + \sum_{k=1}^N a_{ijk} x_{jk} \quad (5)$$

359

360 with dimensions of:  $i$  singular vectors,  $j$  pressure levels, and  $k$  predictors. The  
 361 parameters are:  $c$ , a constant;  $a$ , regressions coefficients; and  $x$ , predictors. We used  
 362 twelve predictors ( $N=12$ ) and have defined eleven different training sets (containing



363 the  $\mathbf{a}$  coefficients) for the geographical regions of interest. Only a single training set  
 364 can be used in the regression calculation. The predictors and training sets are listed  
 365 in Table 2. Worden et al. (2013) selected the predictors based on their importance  
 366 in the regression technique for parameterizing MOPITT forward model  
 367 transmittances of Edwards et al. (1999). The training sets are derived from a multi  
 368 linear fit using real MOPITT observations. The training set period is the entire year  
 369 2006. Once an AK matrix  $\mathbf{A}$  is predicted, the simulated observation profile from the  
 370 NR can be computed using the retrieval equation:

$$371 \quad 372 \quad \mathbf{y}_r = \mathbf{y}_a + \mathbf{A}(\mathbf{y}_{NR} - \mathbf{y}_a) + \boldsymbol{\varepsilon} \quad (6)$$

373 with  $\mathbf{y}_{NR}$ , the NR profile sampled at the MOPITT vertical resolution, replacing the  
 374 true state profile  $\mathbf{y}_t$  in equation 3. Because MOPITT retrieved values express a CO  
 375 quantity over a pressure layer, we compute a weighted average using the pressure  
 376 thickness of the GEOS-5 vertical CO levels mapped onto the MOPITT grid to produce  
 377  $\mathbf{y}_{NR}$ .  
 378

### 379 380 3.4. Training set method limitations

381 In section 3.3 we applied the method described Worden et al. (2013), to  
 382 reconstruct the averaging kernel matrix. In order to utilize the multi linear  
 383 regression (equation 5), we need pre-calculated coefficients ( $\mathbf{a}_{0,N}$ ) from a multi-  
 384 regression fit derived from real MOPITT observations, that we call training sets  
 385 given in Table 2. In some cases, mostly over the CONUS and Asian megacities, very  
 386 high CO profile concentrations and total CO column amount values can extend  
 387 beyond the boundary values of the data set used to build the training set and hence  
 388 beyond the boundary values of the training set itself. Because of the near linear  
 389 relationship between predictors and predicted AKs (equation 4 and 5), using  
 390 predictors from the model with values that are outside the training set distributions  
 391 may lead to unphysical averaging kernel values, e.g., strong negative values or  
 392 values above unity. This is most likely the case for the CO predictors (CO profile and  
 393 CO total column). In order to prevent predictors that are outside the training set  
 394 range and not to discard a significant amount of simulated observation over  
 395 polluted areas we reduce the CO profile predictor as follows. We calculate the mean  
 396 ( $\mu$ ) and standard deviation ( $\sigma$ ) of the CO profile training sets. If the predicted CO  
 397 profile values ( $p$ ) are above  $\mu+2\sigma$ , the new predictor ( $p'$ ) is then calculated as  
 398 follows:  
 399

$$400 \quad 401 \quad p' = (1-\gamma)(\mu+2\sigma) + \gamma p \quad (7)$$

402 where  $\gamma$  is a weighting coefficient ranging between 0 and 1. Then the scaled CO  
 403 profile is used to recalculate related CO predictors (CO column,  $\text{Cos}(\theta_{sza})/\log_{10}\text{CO}(z)$   
 404 and  $dT(z)/\log_{10}\text{CO}(z)$ ). This allows the simulator to produce reasonable variability  
 405 in measurement sensitivity while still including the high CO cases and without  
 406 generating unphysical averaging kernels. Sensitivity tests during extreme pollution  
 407 events have shown that using  $\gamma>0.2$  produces an unacceptably high frequency of  
 408

409 unrealistic averaging kernel functions. In order to have a robust observation  
 410 simulator which does not produce unphysical averaging kernel values we use  $\gamma=0.1$ .

411

### 412 3.5. Simulated error method

413

414 The regression method described above does not account for simulating  
 415 measurement error (represented by the retrieval error covariance matrix) and  
 416 retrieval noise. In order to simulate the error terms, we use the relationships  
 417 between the AK matrix and the associated retrieval errors terms (Rodgers, 2000).  
 418 The associated retrieval noise  $\varepsilon$  is defined using the retrieval noise covariance  
 419 matrix  $\mathbf{C}_n$ , derived from the retrieval error covariance matrix  $\mathbf{C}_x$ . Where  $\varepsilon$  is the  
 420 vector containing the square root of the diagonal elements of  $\mathbf{C}_n$ , and  $y_{err}$  the  
 421 vector containing the square root of the diagonal elements of  $\mathbf{C}_x$ . The retrieval error  
 422 covariance matrix  $\mathbf{C}_x$  can be decomposed as the sum of two matrices (Deeter et al.  
 423 2011):

424

- 425 • A smoothing error covariance matrix  $\mathbf{C}_s$  that describes the expected error  
 426 arising from differences between the true profile and retrieved profile, and  
 427 which are due to the characteristics of the weighting functions and the  
 428 influence of the a priori covariance matrix.
- 429 • A retrieval noise error covariance matrix  $\mathbf{C}_n$  that quantifies the expected  
 430 errors due to errors in the radiances.

431

432 Then

433

$$434 \quad \mathbf{C}_x = \mathbf{C}_s + \mathbf{C}_n \quad (8)$$

435

436 with  $\mathbf{C}_s$  approximated using the a priori covariance matrix  $\mathbf{C}_a$ , as follows

437

$$438 \quad \mathbf{C}_s = (\mathbf{I} - \mathbf{A})\mathbf{C}_a(\mathbf{I} - \mathbf{A})^T \quad (9)$$

439

440 and  $\mathbf{C}_x$  directly calculable from  $\mathbf{C}_a$  and  $\mathbf{A}$

441

$$442 \quad \mathbf{C}_x = (\mathbf{I} - \mathbf{A})\mathbf{C}_a \quad (10)$$

443

444 so that

445

$$446 \quad \mathbf{C}_n = \mathbf{C}_x(\mathbf{I} - (\mathbf{I} - \mathbf{A})^T) \quad (11)$$

447

448

449  $\mathbf{C}_n$  is mostly lower than  $\mathbf{C}_s$  but not negligible (see section 5.2 and figure 11).  
 450 Relatively to  $\mathbf{C}_x$ ,  $\mathbf{C}_n$  will increase if  $\mathbf{C}_s$  decrease (if  $\mathbf{A}$  tends to be the identity  $\mathbf{I}$ ). We  
 451 define  $\mathbf{C}_a$  as for the MOPITT v4 and v5 products (Deeter et al., 2010). The a priori  
 452 covariance matrix  $\mathbf{C}_a$  incorporates the same variance value  $C_0$  at all levels, with a  
 453 constant correlation height  $P_c$  over a pressure level  $p$  defining the off-diagonal  
 454 elements. Thus,

455

$$C_{a,ij} = C_0 e^{-((p_i - p_j)/P_c)^2} \quad (12)$$

456  
457  
458 with  $P_c=100$  hPa and  $C_0=(0.3 \log_{10}e)^2$ . In order to simulate the random error  $\varepsilon$ , we  
459 add a pseudo-random noise on each nature run sampled by a predicted AK:

$$\varepsilon = \mathbf{y}_r \mathbf{C}_n^{1/2} \circ \mathcal{N}(0, \mathbf{I}) \quad (13)$$

460  
461  
462 where  $\circ$  denotes the Schur product and  $\mathcal{N}(0, \mathbf{I})$  a matrix following a normal  
463 distribution of means equal 0 and standard deviation equal the identity matrix  $\mathbf{I}$ . We  
464 also calculate the retrieval error profile as follows:

$$y_{err,i} = y_{r,i} \mathbf{C}_{x,i,i}^{1/2} \quad (14)$$

465  
466  
467 Because the smoothing error  $\mathbf{C}_s$  mostly dominates on the error budget (equation 8),  
470 the impact of the random error  $\varepsilon$  is low compared to the retrieval error profile and  
471 hence the accuracy of the retrievals are not significantly impacted.

#### 472 473 4. Impact of clouds

474  
475 Under cloudy conditions, the simplest approach for MOPITT-like  
476 measurements on a GEO platform would be simply to discard cloudy pixels and not  
477 perform retrievals. It is thus important to assess the impact of the cloud coverage on  
478 GEO measurements. In this study, a scene is considered clear when the interpolated  
479 cloud fraction from the NR is lower than 5% of a single footprint. This is the clear-  
480 sky condition used operationally with real MOPITT measurements. Cloud  
481 contaminated footprints with greater than 5% of cloud fraction would be discarded.  
482 Clouds properties are not used to predict AK variability. Figure 6 presents the ratio  
483 of cloud free pixels, over the month of July 2006 for the constellation. The ratio of  
484 cloud free pixels is the number of cloud free observations divided by the total  
485 number of possible observations (i.e., one per hour during one month) for a given  
486 pixel. Figure 9 gives an idea of instantaneous instrument coverage with a 5% cloud  
487 fraction threshold. The GEO-EU displays very few cloud-contaminated areas  
488 whereas the GEO-AS has very few cloud free areas.

489 The cloud-free ratio geographical distribution shows differences between  
490 intra- and inter-continental regions. On average, GEO-EU has the highest ratio  
491 (60%) followed by GEO-US (40%) and GEO-AS (20%). Strong variations of the ratio  
492 are also observed for different weather regimes within each measurement domain.  
493 Mediterranean weather regimes such as western CONUS and the entire  
494 Mediterranean basin exhibit higher ratios, above 80%. Conversely, oceanic,  
495 subtropical and tropical regimes such as northern Europe, southern CONUS and  
496 southeastern Asia have lower ratios, below 20%. Over the GEO-AS field of view,  
497 Korea and Japan exhibit very low ratios around 10% due to East Asian monsoon  
498 effects that provide persistent convective cloud coverage.

499 The value of the cloud free ratio depends on the spatial resolution of the  
500 observation (pixel size) and the cloud fraction threshold used. Figure 7 displays  
501 results of sensitivity tests on pixel size and cloud fraction threshold. We assume that

502 the lowest pixel size simulated is 7 km due to the model horizontal resolution. We  
503 can then increase the pixel size by averaging contiguous grid cells. It is shown here  
504 that with a given cloud fraction threshold, increasing the pixel size reduces the  
505 average cloud free ratio. We perform tests for varying cloud fraction thresholds to  
506 calibrate the assimilated data product. Variations of the cloud free ratio following  
507 variations in the cloud fraction threshold and the pixel size show the same patterns  
508 (but with a different range of values) for the three instruments of the constellation.

509 To explain these patterns we display a specific case (figure 8) as an example  
510 of how the observed coverage changes with the two varying parameters. The case  
511 study presented shows two typical horizontal cloud structures: one of high  
512 granularity located over the eastern part of the plot, which is identified as  
513 convective structures, and the other of low granularity located on the northwest  
514 part of the plot, which is identified as a cold air front. Over low granularity areas,  
515 decreasing the cloud fraction threshold will not increase the cloud-contaminated  
516 area as much as it does over the high granularity areas. As an idealized example, one  
517 can imagine adding pixels around four single separated sparse pixels (a granular  
518 structure) and adding a pixel around a four-by-four pixel area (a non-granular  
519 structure). In the first case, there will be 8 pixels around each of the 4 original  
520 pixels, making a total of 32 additional pixels. In the second case 12 additional pixels  
521 will surround a 2 by 2 square. The increase in area will be larger with the granular  
522 structure than with the non-granular structure.

523 In the more realistic case of our observation simulations, granularity can  
524 vary at different scales and at different times. We found that adjusting the cloud  
525 fraction threshold to 20% for a 42 km pixel size gives comparable statistics of cloud  
526 coverage as with the 5% threshold for a 7 km pixel size (see section 5.3 and figure  
527 12).

528

## 529 5. Simulated GEO constellation measurements

530

### 531 5.1. Simulated sensitivity analysis

532

533 Figure 9 displays the maps of sampled Surface-700 hPa NR and retrieved  
534 partial columns and associated  $DFS_{0,3}$  for the GEO constellation. Looking at  $DFS_{0,3}$   
535 maps first shows that the observation simulator reproduces the variability of  
536 measurement sensitivity over the satellite measurement domains. The maps are  
537 snapshots during daytime, and show strong differences in  $DFS_{0,3}$  between sea and  
538 land due to the different AK training sets used. The land training set simulates multi-  
539 spectral (TIR+NIR) retrieval AKs in contrast to the sea training set that simulates  
540 TIR-only retrievals. The  $DFS_{0,3}$  values between land and sea surfaces are in  
541 agreement with figure 5: instrument sensitivities over land are generally higher  
542 than over sea, because of the availability of multi-spectral simulated retrievals.  $DFS$   
543 variability over land, or over sea only, is also simulated using the multi-regression fit  
544 as described in section 3.3. To describe this variability, we will focus on the analysis  
545 over land. The most obvious variations of  $DFS_{0,3}$  follow orography. The main reason  
546 is the reduction in the number of retrieved levels if surface pressure is lower than,  
547 e.g., 900 hPa. For a constant number of retrieved levels, the variation of the surface  
548 level layer thickness also plays a significant role (represented by the dP predictor;

549 see table 2), and a thinner surface layer will contribute less retrieval sensitivity.  
550 Variations of  $DFS_{0,3}$  can also be correlated to the CO amount in the NR. This  
551 variability is represented with the CO total column and CO profile predictors. CO  
552 abundance is a strong predictor of sensitivity due to the use of  $\log_{10}(\text{VMR})$  retrievals  
553 in MOPITT with corresponding weighting functions that have increasing magnitude  
554 for increasing VMR (Worden et al., 2013). Finally, the temperature profile and  
555 thermal contrast ( $dT$ ) play a significant role in the  $DFS_{0,3}$  variability, as expected for  
556 the TIR contribution in a multispectral instrument. While  $DFS_{0,3}$  depends more on  
557 predictors such as CO column and  $dP$ , all of the predictors in Table 2 add  
558 information to the regression fit, as tested in Worden et al. (2013).

559 Figure 10 shows scatter plots of  $DFS_{0,3}$  versus the main DFS variability  
560 drivers, i.e., parameters mentioned above such as CO concentration,  $dP$  and  $dT$ .  
561 Night and day values are displayed (blue and red, respectively) showing the  
562 expected increase of sensitivity during day (simulating a multispectral retrieval)  
563 compared to night (simulating a TIR-only retrieval). For each region, using an  
564 alternation of day training sets and night training sets, designed to produce  
565 multispectral and TIR-only retrieval AKs, respectively, then simulates a diurnal cycle  
566 of sensitivity. Correlation of  $DFS_{0,3}$  with predictors gives an indication of which  
567 variables in the NR true state will drive measurement sensitivity. However, this is  
568 not a deterministic result since actual sensitivity depends on all the predictors,  
569 together with the distributions of those

570 variables as compared to the training set distributions, indicated by the lines in  
571 Figure 10. Variations in the dependence on predictors can be seen by the different  
572 distributions in Figure 10 for CONUS, Europe and Asia. Over Asia and Europe,  
573 overall CO concentrations from NR show significantly lower as compared to the  
574 training set mean. For Asia, scatter plots do not show any clear dependence between  
575  $DFS_{0,3}$  and CO concentrations. For Europe, the dependence is more marked during  
576 daytime. Lower CO predictor values compared to training set mean might lead to  
577 underestimation of  $DFS_{0,3}$ , however it fits a realistic range of values (from 0.25 to  
578 0.5).

## 579 580 5.2 NR sampling and error budget

581  
582 The difference between the NR CO and the retrieved CO shows higher NR  
583 values than in the simulated retrievals (fig. 9). Retrieved values can be close to the  
584 NR if sensitivity (DFS) is high enough and/or the a priori CO profile is close enough  
585 to the NR. Cases with strong CO plumes in the NR can be identified in figure 9 over  
586 Asia (around  $35^{\circ}\text{N}$  and  $115^{\circ}\text{E}$ ) and over Europe (around  $5^{\circ}\text{E}$  and  $55^{\circ}\text{N}$ ). In the Asian  
587 case, the plume is very well detected in the synthetic retrieval, because over land  
588 GEO-AS has a  $DFS_{0,3}$  above 0.5 and a priori profile concentrations close to the NR  
589 profile (not shown). In the European case, plumes are barely detected because over  
590 sea the GEO-EU has  $DFS_{0,3}$  below 0.3 and the a priori profile concentrations are far  
591 from NR values. In general, retrieved CO concentrations are lower than the NR CO  
592 concentration because a priori values are lower than NR values. In certain cases (see  
593 fig. 9 for Asia around  $110^{\circ}\text{E}$  and  $35^{\circ}\text{N}$ ), the opposite is observed; a priori  
594 concentrations are higher than the NR. The a priori profile, sampled from a lower  
595 resolution MOZART-4 climatology (see section 3.2) does not capture the specific NR

596 high-resolution features. Conversely, polluted areas are represented as relatively  
597 high CO over broad area, which can produce cases where  $y_a$  is higher than  $y_t$ .

598 Figure 11 left panels show scatter plots of NR CO partial columns ( $X_t$ ) versus  
599 retrieved CO partial columns ( $X_r$ ) with night cases (blue) and day cases (red) over  
600 land. In general, night  $X_r$  values are farther from the  $X_t$  compared to the day  $X_r$   
601 values. As explained in section 5.1 and in figure 10,  $DFS_{0,3}$  values are lower during  
602 night than during day. Lower DFS will produce  $X_t$  values that are closer to the a  
603 priori ( $X_a$ ). If  $X_a$  is far from  $X_t$ , the smoothing error ( $X_s$ ) will increase with lower  
604  $DFS_{0,3}$ . Even if  $DFS_{0,3}$  is high (around 0.7),  $X_s$  can be high if  $X_t$  is very far from  $X_a$ . In  
605 the case of GEO-US, values spread by 10-20 DU (Dobson Units) around the  $X_t=X_r$   
606 axis, showing that  $X_a$  can be higher or lower than  $X_t$ . In the case of GEO-EU, the  
607 spread is lower because  $X_t$  is in general close to  $X_a$ . In the case of GEO-AS,  $X_r$  values  
608 are mostly lower than  $X_t$  values, showing that  $X_a$  is generally lower than  $X_t$ .

609 Figure 11 right panel displays scatter plots of  $X_s$  (in % relative to  $X_r$ ) versus  
610 the surface-700hPa partial column retrieval error ( $X_e$ ). We see that  $X_e$  values are in  
611 the range expected from real MOPITT observations: between 15% and 30%.  
612 Following equation 8 and 14, diagonal values of  $C_s$  should be lower or equal to  
613 diagonal values of  $C_x$  and hence  $X_s$  should be lower or equal to  $X_e$  (if  $X_s$  is calculated  
614 as  $X_e$ ). The condition is respected in most of the cases, but some  $X_s$  values are higher  
615 than  $X_e$ . Again, this happens when  $X_a$  is very distant from  $X_t$ , and due to the fact that  
616  $X_a$  and  $X_t$  (i.e.,  $y_a$  and  $y_t$ ) are not used in the calculation of the a priori covariance  
617 matrix (see section 3.5 and equation 9 and 12). The perfect estimate of  $C_s$  would  
618 then be:

$$619 \quad C_s = (I - A)(y_a - y_t)(y_a - y_t)^T(I - A)^T \quad (15)$$

622 This can be estimated for this study since we are assuming the NR is the true state.  
623 However, for real observations it is not possible to estimate the actual smoothing  
624 covariance error matrix. Therefore, use of the method described in section 3.5 is  
625 more realistic, and will provide reasonable error estimates in most cases since  $X_s$   
626 has generally lower values than  $X_e$ .

### 627 5.3. Reduced resolution simulated observations

630 In part II of this study, we will assimilate the simulated GEO-constellation  
631 into a global model. We will use the global chemistry - climate model CAM-Chem,  
632 including its full chemical scheme (Lamarque et al., 2012). State-of-the-art global  
633 atmospheric chemical models do not have high horizontal resolution. In this second  
634 part of the study, we use a  $0.9^\circ$  by  $1.25^\circ$  resolution model configuration. Since the  
635 resolutions of the NR and the simulated observations are much finer than the CAM-  
636 Chem resolution, we will use the reduced resolution NR ( $0.5^\circ$ , i.e., 42 km  
637 approximately). The reduced NR simulations are the same as the native NR  
638 simulations, but the horizontal resolution has been reduced a posteriori (see Da  
639 Silva et al., 2014).

640 Figure 12 displays the reduced resolution (42 km) simulated observations.  
641 As explained in section 3.5, because the model resolution is 42 km we assume that  
642 the pixel size has the same size. To generate an appropriate sampling according to

643 the pixel resolution, we divide by a factor of 5 the number of latitude and longitude  
644 pixels provided in the table. The left panels show the average surface-700hPa  
645 retrieved CO column for July 2006. The right panels show the cloud free ratio for  
646 July 2006. For the cloud fraction threshold, we use 20% to keep the same cloud free  
647 ratio as for the high-resolution observation simulation, as explained in section 3.5.  
648 Cloud free ratio maps (figure 12) at low resolution are then very similar to the same  
649 maps at high resolution (figure 6).

650  
651

## 652 6. Conclusion

653

654 This paper is Part 1 of a two-part study. Here, we demonstrate the feasibility  
655 of simulating a GEO constellation for air quality monitoring, with a focus on CO.  
656 Three potential instruments are simulated covering the three most populated and  
657 polluted areas of the world: Continental US (CONUS), Western Europe and Eastern  
658 Asia. We use very high-resolution output ( $0.06^\circ$ , i.e.,  $\sim 7$  km horizontal resolution)  
659 from the GEOS-5 model as a NR to simulate a MOPITT-like instrument. Instead of  
660 using a full radiative transfer model to simulate the instrument vertical retrieval  
661 sensitivity as defined by the AK, we use a novel method described by Worden et al.,  
662 (2013). This method employs multi-linear regression using predictors (from the  
663 NR) and training set coefficients (from real MOPITT data) to produce scene-  
664 dependent AKs, thus allowing a very fast computation of the instrument synthetic  
665 measurement dataset. Thus, we avoid the computational burden of using a full  
666 radiative transfer model, allowing the generation of one month of GEO constellation  
667 data in less than 12 hours. This makes simulation of the GEO constellation  
668 measurement computationally feasible. The main conclusions of this work are as  
669 follows:

670

- 671 1. Instead of using the model resolution as the instrument pixel resolution, and  
672 the defined field of view as a simple latitude/longitude rectangle, we present  
673 a method to simulate the data using a GEO projection. This gives accurate  
674 GEO instrument spatial resolutions and fields of view that vary with latitude  
675 and longitude.
- 676 2. This paper extends application of the Worden et al., (2013) averaging kernel  
677 (AK) prediction method. Realistic variations of potential GEO instrument  
678 vertical retrieval sensitivities are simulated. Instrument sensitivities depend  
679 on predictors and the main drivers are: surface pressure, CO profile and  
680 temperature profile. Rather than using an average AK for fast computation,  
681 the observation simulator presented here is able to provide fast computation  
682 of AK variability (and its associated retrieval error covariance matrix) at the  
683 same time.
- 684 3. We discuss limitations of the method used for this study. The very high CO  
685 concentrations occurring in the NR over very polluted areas often overreach  
686 the training set statistical coverage. In this situation, we use a tuning method  
687 to reduce the amplitude of CO variations in the NR.
- 688 4. To make the observation simulations as realistic as possible, we account for  
689 the impact of clouds. Cloud contamination in the observations is strongly

690 dependent on the instrument spatial resolution and the geographical region  
691 of interest. The Mediterranean weather regimes show the lowest cloud  
692 occurrences, whereas subtropical weather might provide comparatively  
693 lower temporal and spatial sampling for air quality GEO measurements.

694 5. We present case studies for the three measurement domains and show that  
695 the observation simulation method employed here provides realistic AK  
696 variability. The degrees of freedom for signal for the lowermost troposphere  
697 ( $DFS_{0-3}$ ) ranges from 0.2 to 0.7 with significantly larger values over land and  
698 for day that reflect the enhanced vertical sensitivity possible with  
699 multispectral retrievals. We simulate small local  $DFS_{0-3}$  variations according  
700 to surface and atmospheric parameters (e.g., surface pressure, CO profile and  
701 temperature profile).

702 6. Simulated retrieval errors that are derived from the AK simulation are  
703 compared to the true smoothing error. Comparisons show that the retrieved  
704 errors are realistic, being lower than or in the range of the smoothing error.

705

706 The next step in this study (Part 2) will be to assimilate the synthetic  
707 measurement data into a global model. To do so, we present here an additional set of  
708 simulated observations at a reduced spatial resolution (42 km). This allows an OSSE  
709 for the potential future prediction system of global air quality with the same  
710 capabilities for each region of interest: the same models (NR and CR), the same data  
711 assimilation system (AS) and the same instrument design (observation simulator).  
712 The goals of Part 2 will be to: (1) assess the ability of the GEO constellation to observe  
713 the impact of pollutant emissions over each region; (2) look at the importance of  
714 long-range transport between regions; and (3) investigate the value of the  
715 measurements from each mission in the GEO constellation, taken individually and  
716 together.

717

718

719 Acknowledgements: This work was partly supported by NASA grants  
720 NNX09AH03G S02, NNX11AI10G and NNX11AG63G. The National Center for  
721 Atmospheric Research is sponsored by the National Science Foundation.

722

723

724 References:

725

726 Bowman, K. W.: Toward the next generation air quality monitoring: Ozone.  
727 *Atmospheric Environment* 80: 571–583. 10.1016/j.atmosenv.2013.07.007. 2013.

728

729 Committee on Earth Observation Satellites (CEOS), Atmospheric Composition  
730 Constellation: A Geostationary Satellite Constellation for Observing Global Air  
731 Quality: An International Path Forward, [http://old.ceos.org/images/ACC/AC\\_Geo\\_Position\\_Paper\\_v4.pdf](http://old.ceos.org/images/ACC/AC_Geo_Position_Paper_v4.pdf), April 12, 2011

732

733 Claeysman, M., Attié, J.-L., Peuch, V.-H., El Amraoui, L., Lahoz, W. A., Josse, B.,  
734 Ricaud, P., von Clarmann, T., Höpfner, M., Orphal, J., Flaud, J.-M., Edwards, D. P.,  
Chance, K., Liu, X., Pasternak, F., and Cantié, R.: A geostationary thermal infrared



- 735 sensor to monitor the lowermost troposphere: O<sub>3</sub> and CO retrieval studies, *Atmos.*  
736 *Meas. Tech.*, 4, 297-317, doi:10.5194/amt-4-297-2011, 2011.
- 737 da Silva, A.M., W. Putman and J. Nattala: File Specification for the 7-km GEOS-5  
738 Nature Run, Ganymed Release (Non-hydrostatic 7-km Global Mesoscale Simulation).  
739 GMAO Office Note No. 6 (Version 1.0), 176 pp, available from  
740 [http://gmao.gsfc.nasa.gov/pubs/office\\_notes](http://gmao.gsfc.nasa.gov/pubs/office_notes). 2014.
- 741 Deeter, M. N., et al., The MOPITT version 4 CO product: Algorithm enhancements,  
742 validation, and long-term stability, *J. Geophys. Res.*, 115, D07306,  
743 doi:10.1029/2009JD013005. 2010.
- 744  
745 Deeter, M. N., H. M. Worden, J. C. Gille, D. P. Edwards, D. Mao, and J. R. Drummond,  
746 MOPITT multispectral CO retrievals: Origins and effects of geophysical radiance  
747 errors, *J. Geophys. Res.*, 116, D15303, doi:10.1029/2011JD015703. 2011.
- 748  
749 Deeter, M. N., Martinez-Alonso, S., Edwards, D. P., Emmons, L. K., Gille, J. C., Worden,  
750 H. M., Pittman, J. V., Daube, B. C., and Wofsy, S. C.: Validation of MOPITT Version 5  
751 thermalinfrared, near-infrared, and multispectral carbon monoxide profile  
752 retrievals for 2000–2011, *J. Geophys. Res.-Atmos.*, 118, 1– 16,  
753 doi:10.1002/jgrd.50272, 2013.
- 754  
755 Drummond, J. R., Measurements of Pollution in the Troposphere (MOPITT), in *The*  
756 *Use of EOS for Studies of Atmospheric Physics*, edited by J. C. Gille and G. Visconti,  
757 pp. 77–101, North-Holland, New York. 1992.
- 758  
759 Edwards, D. P., Halvorson, C. M., and Gille, J. C.: Radiative transfer modeling for the  
760 EOS Terra satellite Measurement of Pollution in the Troposphere (MOPITT)  
761 instrument, *J. Geophys. Res.*, 104, 16755–16775, 1999.
- 762  
763 Edwards, D. P., Arellano Jr., A. F., and Deeter, M. N.: A satellite observation system  
764 simulation experiment for carbon monoxide in the lowermost troposphere, *J.*  
765 *Geophys. Res.*, 114, D14304, doi:10.1029/2008JD011375, 2009.
- 766  
767 Emmons, L. K., et al., Description and evaluation of the Model for Ozone and Related  
768 chemical Tracers, version 4 (MOZART-4), *Geosci. Model Dev.*, 3, 43–67. 2010.
- 769  
770 EUMETSAT, The EUMETSAT Satellite Application Facility on Land Surface Analysis,  
771 Product User Manual, Issue 2.6 v2, Météo-France-CNRM. 2011.
- 772  
773 Fishman, J., et al., The United States' Next Generation of Atmospheric Composition  
774 and Coastal Ecosystem Measurements: NASA's Geostationary Coastal and Air  
775 Pollution Events (GEO-CAPE) Mission. *Bull. Amer. Meteor. Soc.*, 93, 1547–1566. doi:  
776 <http://dx.doi.org/10.1175/BAMS-D-11-00201.1>. 2012
- 777  
778 Kaiser, J. W. , A. Heil, M. O. Andreae, A. Benedetti, N. Chubarova, L. Jones, J.-J.  
779 Morcrette, M. Razinger, M. G. Schultz, M. Suttie, and G. R. van der Werf, 2012:

- 780 Biomass burning emissions estimated with a global fire assimilation system based  
781 on observed fire radiative power. *Biogeosciences*, 9(1):527–554, 2012. doi:  
782 10.5194/bg-9-527-2012.
- 783
- 784 Lahoz, W. A., et al., Monitoring Air Quality from Space: The Case for the  
785 Geostationary Platform. *Bull. Amer. Meteor. Soc.*, **93**, 221–233. doi:  
786 <http://dx.doi.org/10.1175/BAMS-D-11-00045.1>. 2012
- 787
- 788 Lamarque, J.-F., Emmons, L. K., Hess, P. G., Kinnison, D. E., Tilmes, S., Vitt, F.,  
789 Heald, C. L., Holland, E. A., Lauritzen, P. H., Neu, J., Orlando, J. J., Rasch, P. J., and  
790 Tyndall, G. K.: CAM-chem: description and evaluation of interactive atmospheric  
791 chemistry in the Community Earth System Model, *Geosci. Model Dev.*, 5, 369–411,  
792 doi:10.5194/gmd-5-369-2012, 2012.
- 793
- 794 Olivier, J., A. Bouwman, C. Maas, and J. Berdowski: Emission Database for Global  
795 Atmospheric Research (EDGAR). *Environ. Monit. Assess.*, 31, 93–106. 1994.
- 796
- 797 Rienecker et al., The GEOS-5 Data Assimilation System— Documentation of Versions  
798 5.0.1, 5.1.0, and 5.2.0, Technical Report Series on Global Modeling and Data  
799 Assimilation, Volume 27, NASA/TM–2008–104606, Vol. 27, 2008
- 800
- 801 Rodgers, C. D.: *Inverse Methods for Atmospheric Sounding, Theory and Practice*,  
802 World Scientific, Singapore, New Jersey, London, Hong Kong, 2000.
- 803
- 804 Sellitto, P., Dufour, G., Eremenko, M., Cuesta, J., Peuch, V.-H., Eldering, A., Edwards, D.  
805 P., and Flaud, J.-M.: The effect of using limited scene-dependent averaging kernels  
806 approximations for the implementation of fast Observing System Simulation  
807 Experiments targeted on lower tropospheric ozone, *Atmos. Meas. Tech. Discuss.*, 6,  
808 2413–2448, doi:10.5194/amtd-6-2413-2013, 2013a.
- 809
- 810 Sellitto, P., Dufour, G., Eremenko, M., Cuesta, J., Forêt, G., Gaubert, B., Beekmann, M., -  
811 H Peuch, V., and Flaud, J.-M.: Monitoring the lowermost tropospheric ozone with  
812 thermal infrared observations from a geostationary platform: performance analyses  
813 for a future dedicated instrument, *Atmos. Meas. Tech. Discuss.*, 6, 6445–6490,  
814 doi:10.5194/amtd-6-6445-2013, 2013b.
- 815
- 816 Timmermans, R., W.A. Lahoz, J.-L. Attié, V.-H. Peuch, L. Curier, D. Edwards, H. Eskes,  
817 and P. Builtjes : Observing System Simulation Experiments for Air Quality. *Atmos.*  
818 *Env.*, submitted. 2014
- 819
- 820 Worden, H. M., M.N. Deeter, D. P. Edwards, J. C. Gille, J. R. Drummond, and P. Nedelec,  
821 Observations of near-surface carbon monoxide from space using MOPITT  
822 multispectral retrievals, *J. Geophys. Res. Atmos.*, doi:10.1029/2010JD014242. 2010.
- 823
- 824 Worden, H. M., Edwards, D. P., Deeter, M. N., Fu, D., Kulawik, S. S., Worden, J. R., and  
825 Arellano, A.: Averaging kernel prediction from atmospheric and surface state  
826 parameters based on multiple regression for nadir-viewing satellite measurements

827 of carbon monoxide and ozone, *Atmos. Meas. Tech.*, 6, 1633-1646, doi:10.5194/amt-  
828 6-1633-2013, 20, 2013.

829

830 Zoogman, P., Jacob, D. J., Chance, K., Zhang, L., Le Sager, P., Fiore, A. M., Eldering, A.,  
831 Liu, X., Natraj, V., and Kulawik, S. S.: Ozone Air Quality Measurement Requirements  
832 for a Geostationary Satellite Mission, *Atmos. Environ.*, 45, 7143–7150,  
833 doi:10.1016/j.atmosenv.2011.05.058, 2011.

834

835 Zoogman, P., D.J. Jacob, K. Chance, H.M. Worden, D.P. Edwards, L. Zhang, Improved  
836 monitoring of surface ozone air quality by joint assimilation of geostationary  
837 satellite observations of ozone and CO. *Atmospheric Environment*, 84, 254-261,  
838 2014a.

839

840 Zoogman, P., D.J. Jacob, K. Chance, X. Liu, A. Fiore, M. Lin, K. Travis, Monitoring high-  
841 ozone events in the US Intermountain West using TEMPO geostationary satellite  
842 observations. *Atmospheric Chemistry and Physics*, 14, 6261-6271, 2014b.

843

844

845

846

847

848

849

850

851

852

853

854

855

856

857

858

859

860

861

862

863

864

865

866

867

868

869

870

871

872

873

874  
875  
876  
877

Tables:

	GEO-AM	GEO-EU	GEO-AS
Sub_lon	-97°	8.4°	120°
Number x pixels	500	400	400
Number y pixels	230	250	200
X <sub>max</sub>	3.5°	2.4°	3.3°
X <sub>min</sub>	-3.5°	-2.4°	-3.3°
Y <sub>max</sub>	7.2°	8.2°	6.7°
Y <sub>min</sub>	4.2°	5.7°	3.5°

878  
879  
880  
881  
882  
883  
884  
885  
886

**Table 1. GEO-constellation instrument specifications: satellite position, number of pixels and angles of views.**

Predictors	Training sets
$\theta_{sza}$	North Hemisphere Ocean (TIR)
Emissivity	CONUS Day (Psrf>900hPa, TIR+NIR)
Latitude	CONUS Night (Psrf>900hPa, TIR)
Surface temperature	Europe Day (Psrf>900hPa, TIR+NIR)
$dP=P_{surface}-P_{ref}^*$	Europe Night (Psrf>900hPa, TIR)
CO column	Eastern Asia Day (Psrf>900hPa, TIR+NIR)
Water Vapor Q(z)	Eastern Asia Night (Psrf>900hPa, TIR)
CO(z)	N.H. Mountains Day (900hPa>Psrf>800hPa, TIR+NIR)
Thermal contrast $dT(z)=(T_{srf}-T(z))$	N. H. Mountains Day (800hPa>Psrf>700hPa, TIR)
$dT(z)^2$	N.H. Mountains Night (900hPa>Psrf>800hPa, TIR+NIR)
$\cos(\theta_{sza})/\log_{10}CO(z)$	N. H. Mountains Night (800hPa>Psrf>700hPa, TIR)
$dT(z)/\log_{10}CO(z)$	

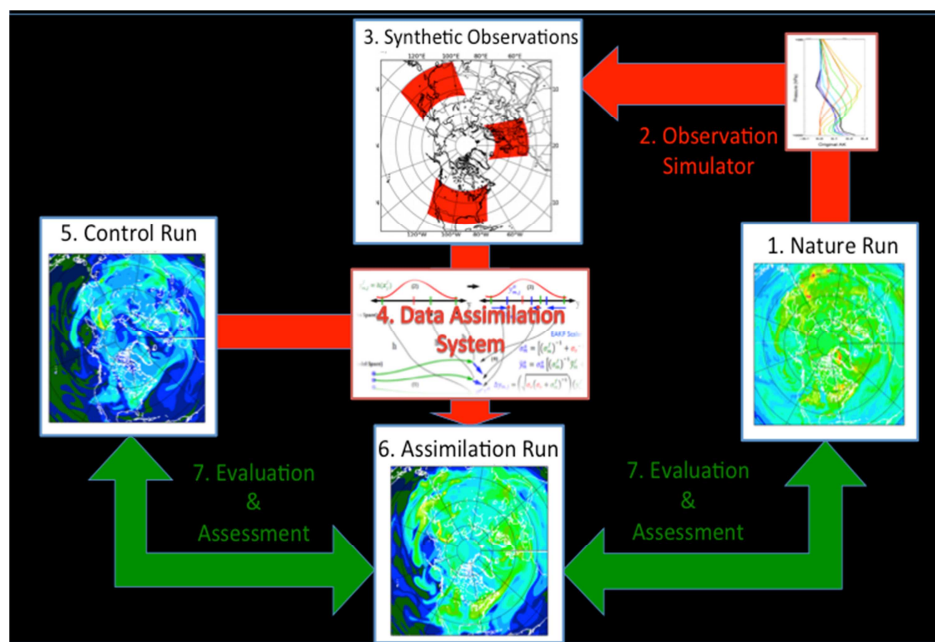
887  
888  
889  
890  
891  
892  
893  
894  
895  
896  
897  
898  
899

\*P<sub>ref</sub>=1000hPa

**Table 2. Left: List of predictors, right: List of the different training sets used to produce the geostationary constellation CO measurements. TIR and NIR state if the training set simulates multispectral or TIR-only retrievals (see text for details).**

900  
901  
902  
903  
904  
905  
906

Figures:



907  
908  
909  
910  
911  
912  
913  
914

Figure 1. The chemical OSSE framework. See text for details.

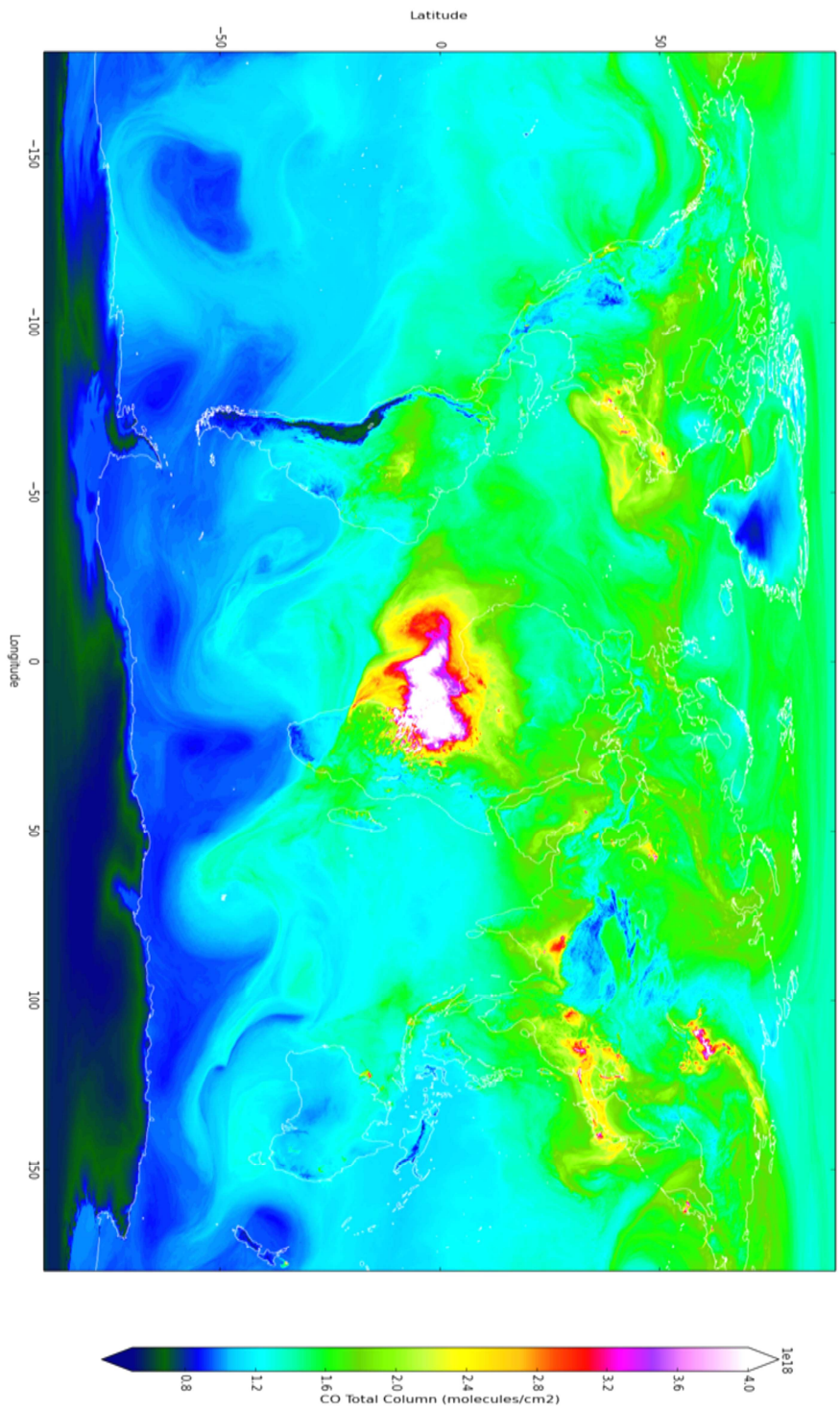
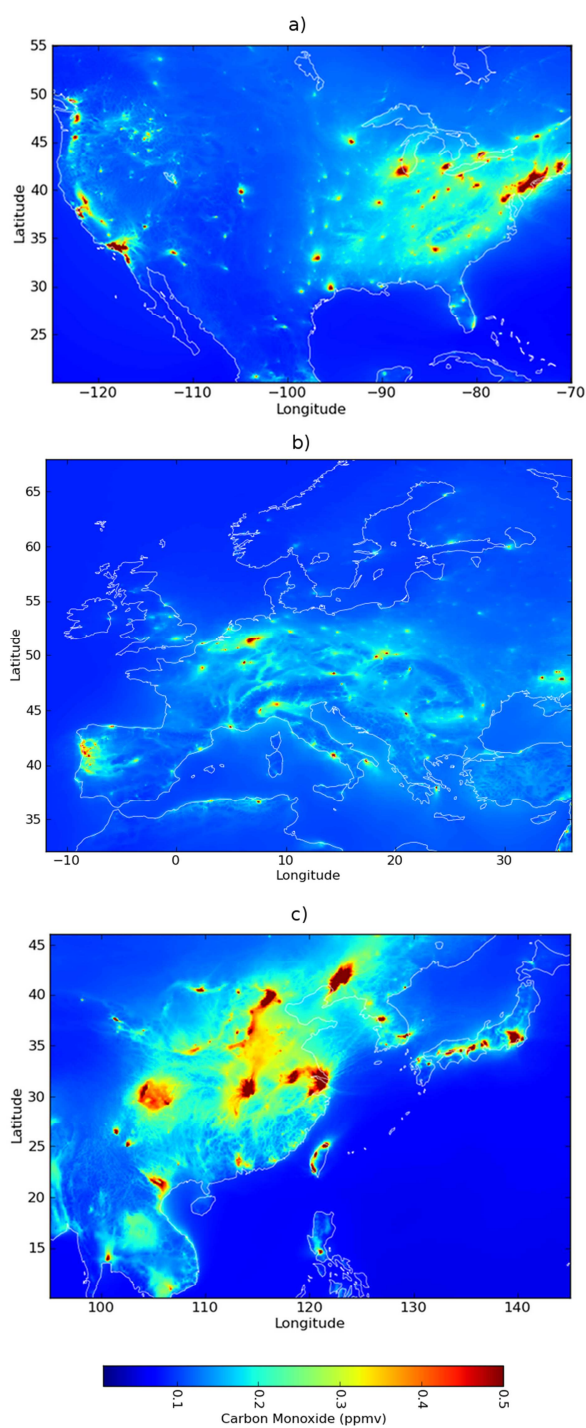
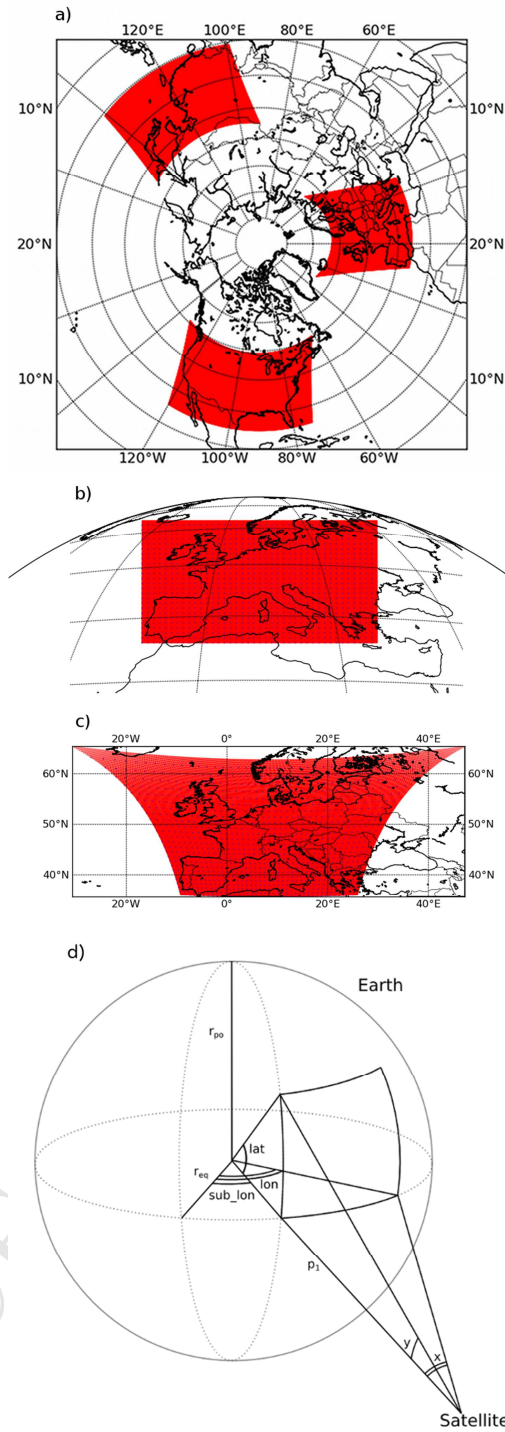


**Figure 2. Total carbon monoxide column in molecules/cm<sup>2</sup> from the GEO5-5 7km resolution Nature Run, 15 July 2006 15:00 UT.**

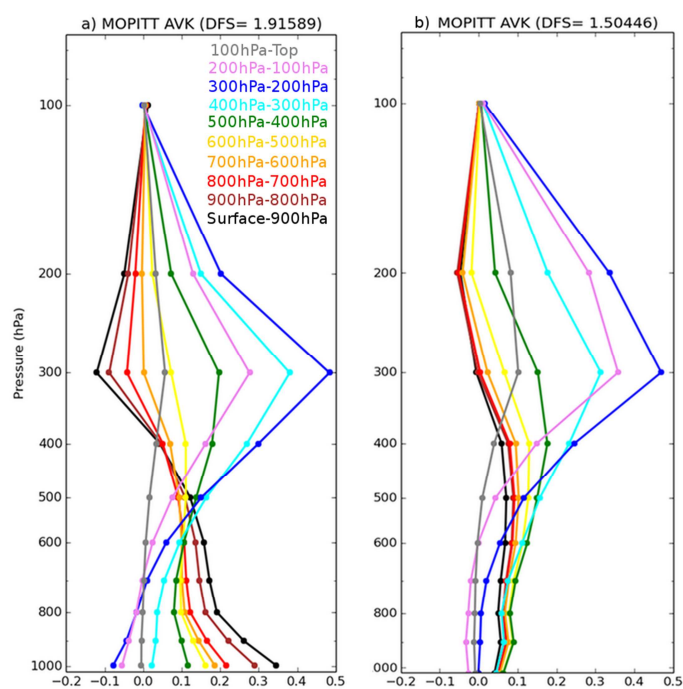


916  
917 **Figure 3. Surface CO time average during July 2006 over (a) North America, (b)**  
918 **Europe, and (c) Asia.**  
919  
920



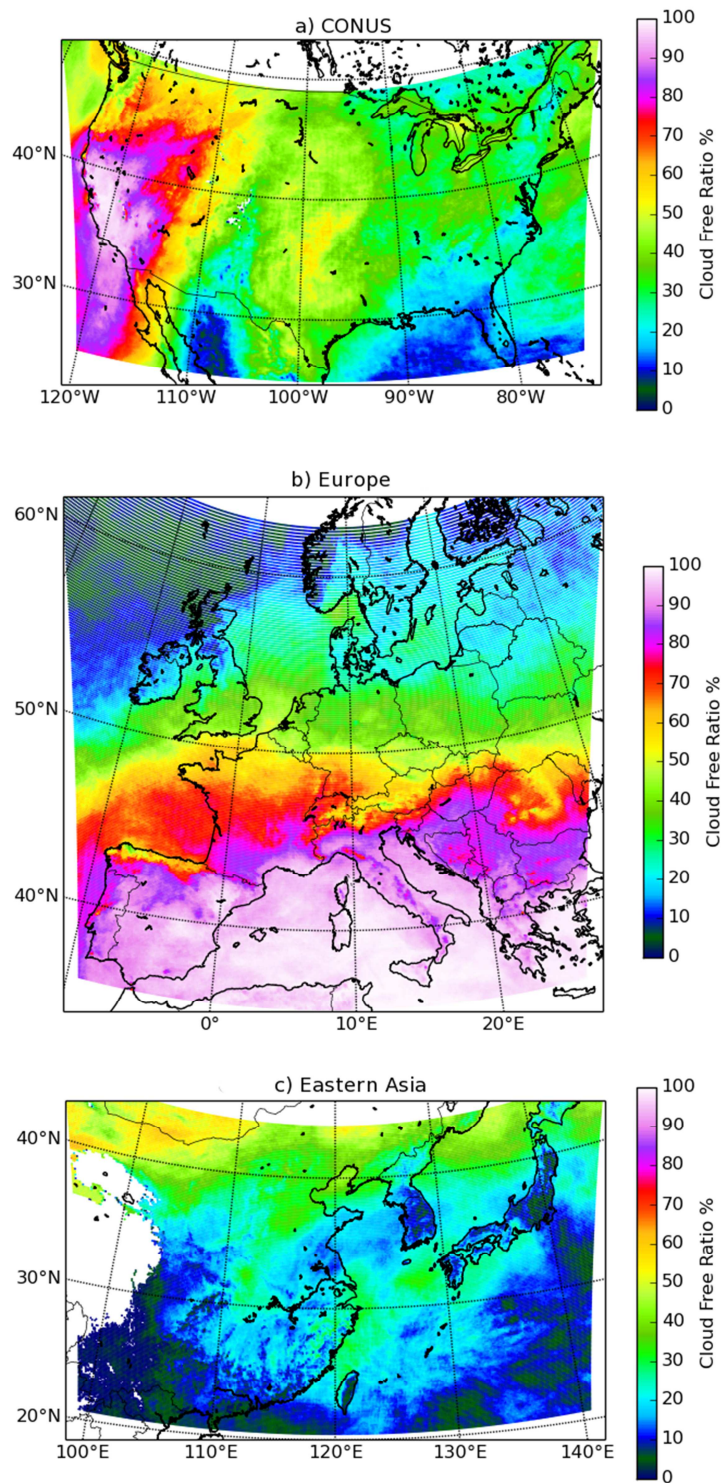
921  
 922 **Figure 4. a) Geostationary constellation measurement domain a) Polar**  
 923 **projection. b) GEO-EU domain in a geostationary projection, red dots are the**  
 924 **full resolution footprints, purple dots are plotted every 100<sup>th</sup> pixels. c) is the**  
 925 **same as b) but in an equidistant latitude-longitude cylindrical projection. d)**  
 926 **Geometrical sketch of the geostationary projection.**  
 927





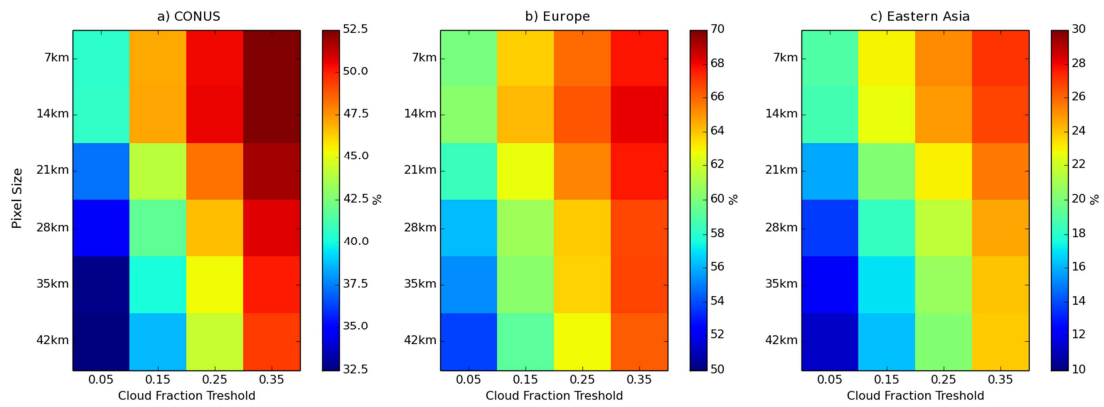
928  
929  
930

**Figure 5. Examples of original typical MOPITT averaging kernels (AKs). Left panel: multispectral day/land AK. Right panel: night/land or sea AK.**



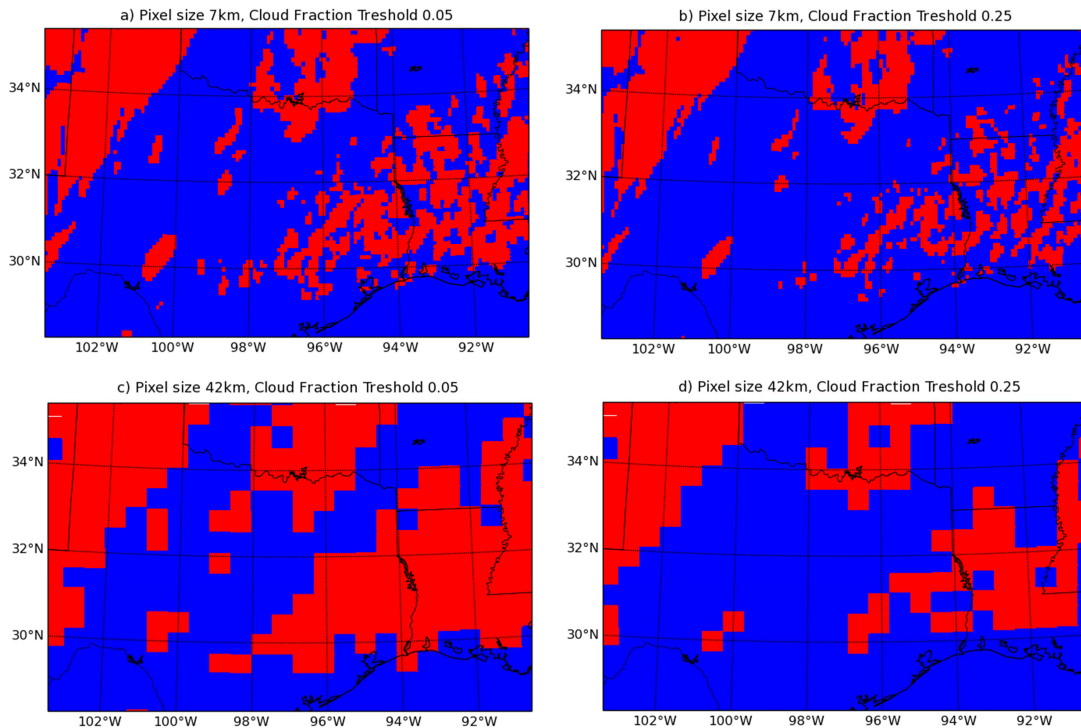
931  
932  
933

**Figure 6. Cloud free ratio (%) for the three measurement domains during July 2006.**



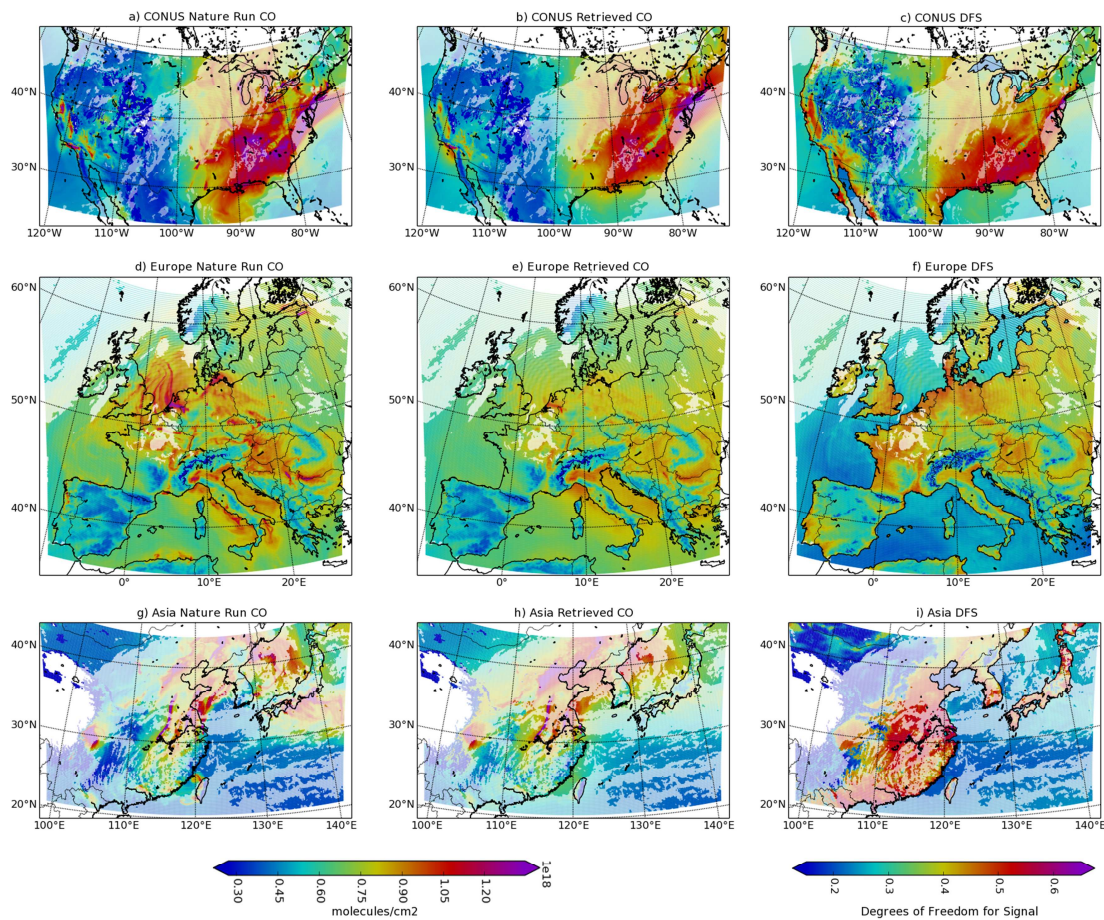
934  
935  
936  
937  
938

**Figure 7. Sensitivity matrices of the average cloud free ratio (in %) for pixel size versus cloud fraction threshold.**



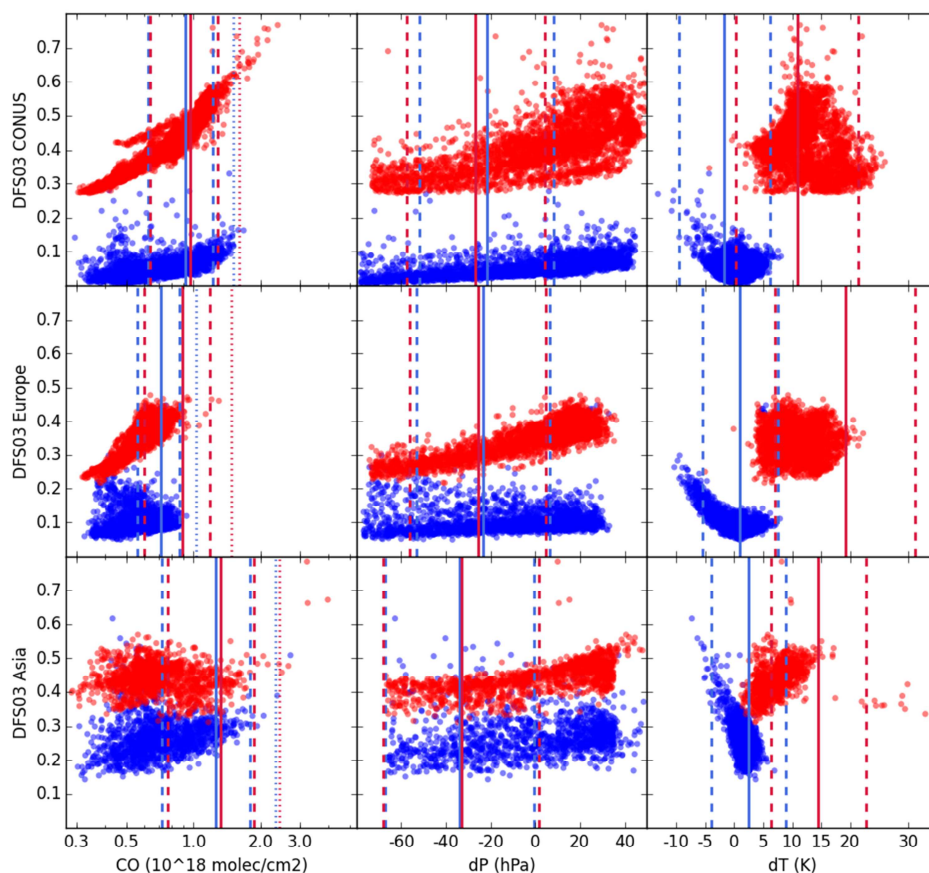
939  
940  
941  
942  
943  
944  
945  
946  
947

**Figure 8. Examples of cloud detection and ratio of observed area for two different cloud fraction thresholds and two different pixel sizes. Red are cloud contaminated pixels and blue are cloud free pixels. Performed over South East CONUS 5 July 2006 00UT.**



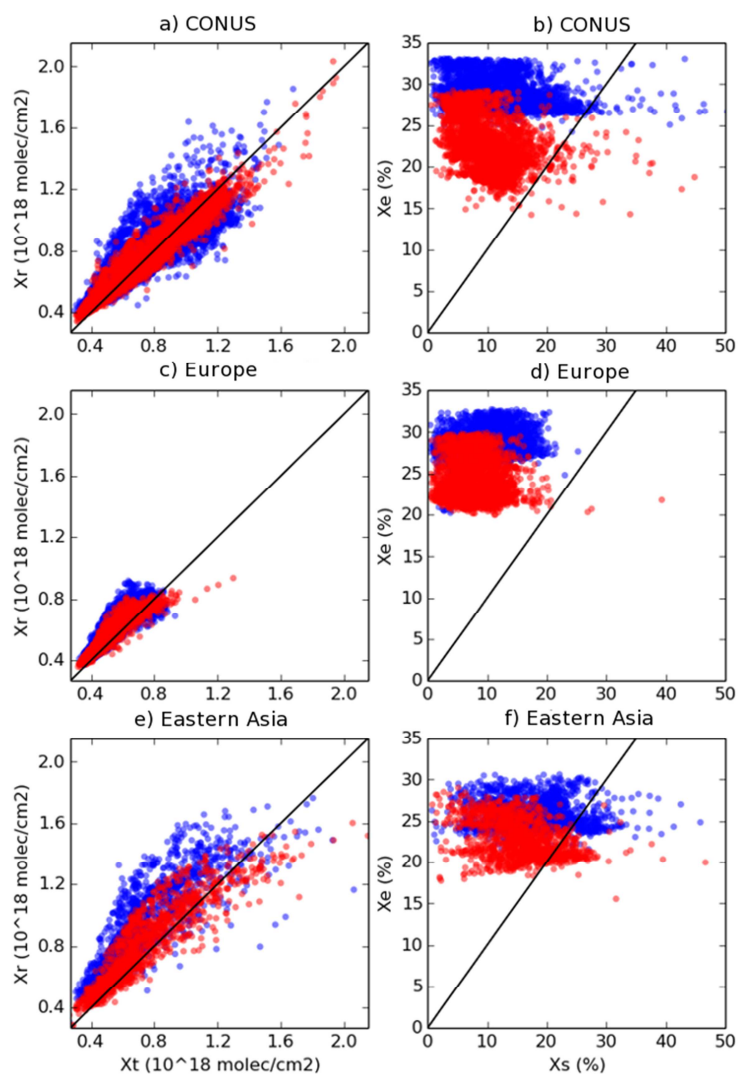
948  
949  
950  
951  
952  
953  
954  
955  
956

**Figure 9. Snapshots of the Nature Run surface to 700 hPa partial column (a, d, g). Corresponding retrieved partial column (b, e, h) and corresponding degrees of freedom for signal (DFS) for surface to 700 hPa (c, f, j). Snapshots are captured at daytime but different dates following regions: 4 July 2006 02UT CONUS, 14 July 2006 10UT Europe, 22 July 2006 18UT Eastern Asia. Deep colors are the cloud-free pixels. Faded colors represent cloud-contaminated pixels that are not used in further processing.**



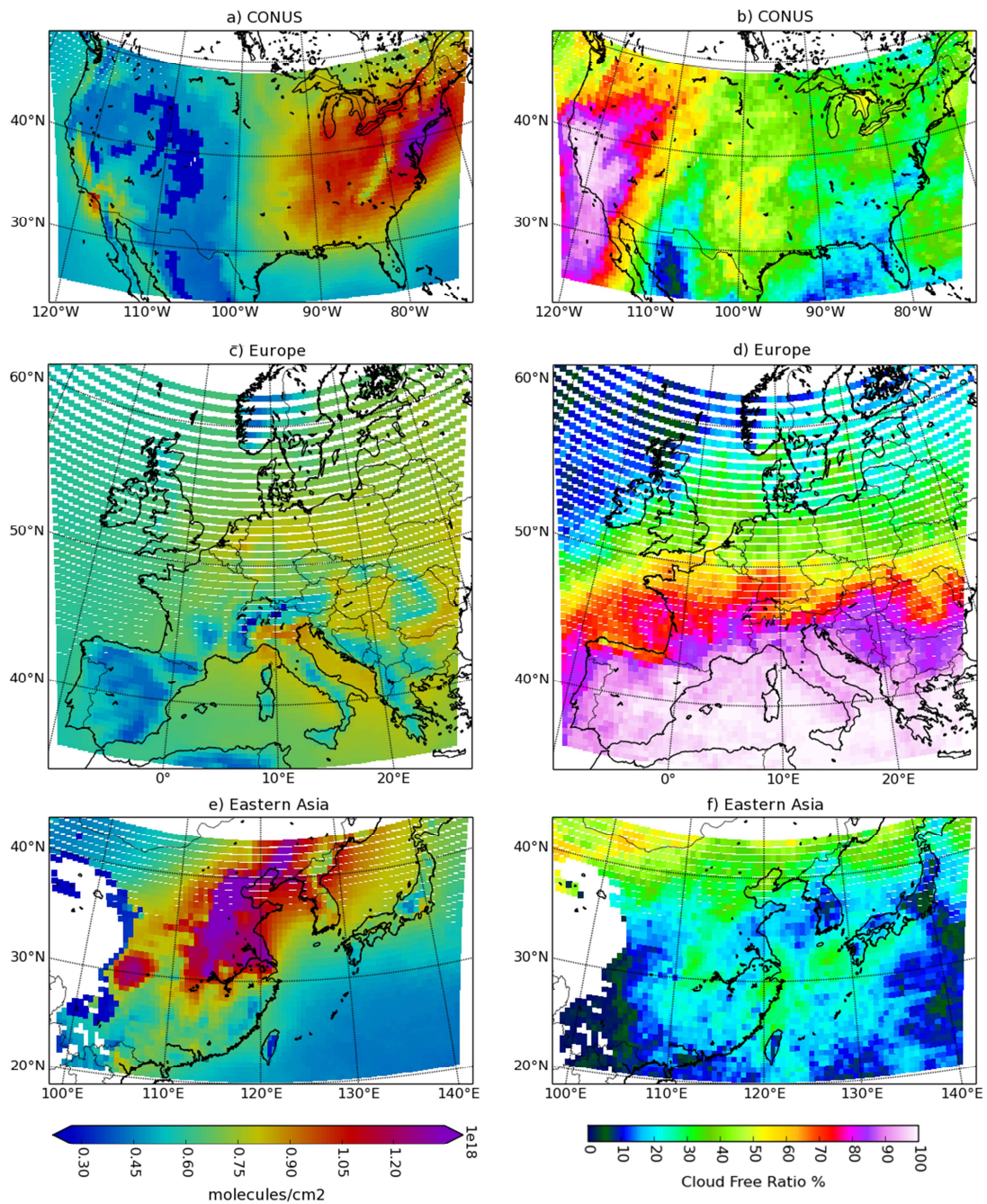
957  
 958  
 959  
 960  
 961  
 962  
 963  
 964

**Figure 10. Scatter plots showing variation of degrees of freedom for signal of surface to 700 hPa versus predictors with highest impacts to the multi-linear regression fit (see table 2 and text for details). Red are day-time values (3pm local time) and blue are night-time values (3am local time) 5 July 2006. Vertical solid lines indicate the mean value of the distribution used to build the training sets and dashed lines indicate associated  $\pm\sigma$  (standard deviation). Dotted lines indicate associated  $+2\sigma$  for CO training set.**



965  
 966  
 967  
 968  
 969

**Figure 11. Left panels: scatter plots of Nature run surface-700 hPa partial columns ( $X_t$ ) versus corresponding retrieved partial columns ( $X_r$ ). Right panels: Smoothing error ( $X_s$ ) versus corresponding retrieved error ( $X_e$ ). Dates are the same as described in figure 10.**



970  
971  
972  
973  
974

**Figure 12. Low-resolution observation simulations used for the assimilation runs. Left panels: July 2006 average retrieved CO surface-700 hPa partial column. Right panels: Cloud free ratio for July 2006.**

**Highlights**

- A constellation of geostationary platforms for mapping pollutant sources and variability is described
- Observation simulation without radiative transfer model is computationally cheap
- Impacts of clouds are diagnosed and is dependent of the weather regime
- A detailed analysis of the simulated observation sensitivity is performed
- Limitations of the method are discussed